

EES Batteries

Accepted Manuscript

This article can be cited before page numbers have been issued, to do this please use: A. R. T. Morrison, W. Dawson, H. Reid, J. Li, I. Mombrini, R. S. Young, A. V. Llewellyn, G. Giri, P. P. Paul, A. Boyce, R. Jervis, J. Robinson, T. Miller, E. Kendrick, P. J. Withers, M. di Michiel, D. J. Brett and P. Shearing, *EES Batteries*, 2026, DOI: 10.1039/D6EB00017G.



This is an Accepted Manuscript, which has been through the Royal Society of Chemistry peer review process and has been accepted for publication.

Accepted Manuscripts are published online shortly after acceptance, before technical editing, formatting and proof reading. Using this free service, authors can make their results available to the community, in citable form, before we publish the edited article. We will replace this Accepted Manuscript with the edited and formatted Advance Article as soon as it is available.

You can find more information about Accepted Manuscripts in the [Information for Authors](#).

Please note that technical editing may introduce minor changes to the text and/or graphics, which may alter content. The journal's standard [Terms & Conditions](#) and the [Ethical guidelines](#) still apply. In no event shall the Royal Society of Chemistry be held responsible for any errors or omissions in this Accepted Manuscript or any consequences arising from the use of any information it contains.

SCHOLARONE™
Manuscripts

Open Access Article. Published on 07 April 2026. Downloaded on 4/8/2026 9:04:09 AM.
This article is licensed under a Creative Commons Attribution 3.0 Unported Licence.



EES Batteries Accepted Manuscript

Conventionally designed battery electrodes are limited to trade-off energy and power density. This trade-off limits how batteries can be deployed, which limits in which use cases they can be employed to enable the energy transition. Our work seeks to understand a strategy for breaking this trade-off by structuring electrodes to add lithium highways to speed transport. We accomplish this with a new application of a specialized x-ray diffraction (XRD) technique, called “multi-channel collimator XRD” that can obtain XRD data from a spatially localized area (10 μm x 10 μm x 670 μm). This allows us to probe the lithiation state of the cathode near and far from these lithium highways, and to elucidate the way that lithium moves through the structure. Understanding lithium movement through these electrodes on a fine scale is essential for rational design, which is the only way to access their full potential. Our work shows this XRD technique is an ideal way to study systems like these, and we expect future research to utilize it in a similar manner in related areas. On a concrete level, it will enable electrode designed with both capacity and power, allowing for another expansion of how batteries can be employed.

[View Article Online](#)

DOI: 10.1039/D6EB00017G



Understanding energy-power trade-off in the structure of li-ion battery cathodes by localized operando XRD

View Article Online
DOI: 10.1039/D6EB00017G

Andrew R.T. Morrison^{1,2,*}, Will J. Dawson^{1,2,3}, Hamish T. Reid^{1,3}, Juntao Li^{2,9}, Isabella Mombrini^{1,4}, R. S. Young^{1,2}, Alice V. Llewellyn^{1,2}, Gargi Giri^{1,2,9}, Partha P. Paul^{4,5}, Adam M. Boyce⁶, Rhodri Jervis^{1,2,3}, Thomas S. Miller^{1,2,3}, James B. Robinson^{1,2,3}, Emma Kendrick^{2,7}, Philip J. Withers⁵, Marco di Michiel⁴, Dan J.L. Brett⁸, Paul R. Shearing^{2,9,*}

1: *Electrochemical Innovation Lab, University College London, London, WC1E 7JE, UK*

2: *The Faraday Institution, Didcot, OX11 0RA, UK*

3: *Advanced Propulsion Lab, UCL East, University College London, London E20 2AE, UK*

4: *ESRF – The European Synchrotron, 71 Av. des Martyrs, 38000 Grenoble, France*

5: *Henry Royce Institute, Dept of Materials, University of Manchester, Manchester M1 3BB, UK*

6: *School of Mechanical and Materials Engineering, University College Dublin, Dublin D04V1W8, Ireland*

7: *School of Metallurgy and Materials, University of Birmingham, Edgbaston, Birmingham, BT15 2TT, UK*

8: *Prosemino Ltd, Paper Yard, Quebec Way, London SE16 7LG*

9: *The ZERO Institute University of Oxford., Holywell House, Osney Mead, Oxford, OX2 0ES*

*: *Corresponding Authors*

Abstract

Power and energy density represent a trade-off in design of lithium-ion batteries at several scales. At the electrode scale this is because for high energy density, thick electrodes are required, and for high power density, thin electrodes are required. It is essentially a mass transport limitation. A strategy to break this trade-off is to develop structured - electrodes with regions of lower tortuosity (e.g. cracks or channels) that can alleviate the mass transport limitations of thick electrodes. However, to achieve a rational design of such electrodes a greater understanding of their inner workings is required. In this study we apply the multi-channel collimator X-ray diffraction technique, which obtains XRD patterns from a specific volume of space, to study a model system for a structured electrode - an NMC622 cathode with pronounced cracking - under operando conditions in a normal coin cell. Probing the local lithiation state near and far from a crack allows us to elucidate mass transport of lithium ions in the electrode and show how the mass transport problem cannot be separated from the electrochemical.

Introduction

Batteries are an example of a technology that has both immediate industrial relevance, with the battery market being large and only growing,¹ and key long-term technology goals, featuring prominently in strategies for the transition to a carbon free energy economy^{2,3}. In this respect, lithium-ion batteries (LIB) dominate both the current market place and research and development of battery technology because the high energy density has opened up many applications.⁴ Even so, it remains challenging to achieve a high-power density along with a high energy density.

This is due to the power-energy trade-off in LIB electrodes design - an electrode designed for high energy density will have a low charge/discharge rate and vice-versa.⁵ A result of this is seen in LIB manufacturers offering the same form factor of cell with different optimisation for power and energy.⁵ The mechanisms behind the power-energy trade-off are manifold including contributing factors like current collector thickness and the intrinsic rate/density profiles of different active materials.^{6,7} Active material particle level effects where, for example, heterogeneous lithiation profiles and particle level cracking can be very important here.⁸⁻¹³ However, for the purposes of this work, the interesting feature is the overall



structure of the electrode, not particle level phenomena. To achieve high energy density in traditionally manufactured electrodes typically requires the electrodes to be thick,⁶ for the maximization of the weight fraction of the electrode which is active material.¹⁴ However, thick electrodes impose limitations on rate because of the long, tortuous diffusion pathways lithium ions must follow. Eventually, above a certain rate the regions of the electrode closest to the current collector become inactive, which has been seen through *operando* X-ray diffraction (XRD)¹⁵ and predicted in models.¹⁶ This highlights the performance limitation associated with the mass transport of lithium ions through the electrolyte within the electrode to near the current collector.

To design electrodes that exceed the power-energy trade-off of slurry cast electrodes, this mass transport limitation of the electrode design must be overcome, which means reducing electrode tortuosity, particularly toward the current-collector. To affect this reduction in tortuosity researchers have tried several strategies to introduce a microstructure that has a bimodal tortuosity distribution. Very low in some regions, while similar to standard electrodes in the rest – bi-tortuous electrodes. In practice these strategies have included templating before casting,¹⁷⁻²⁴ extruding in shapes,^{25, 26} and machining after dry.²⁷⁻³⁰ An alternative to the bi-tortuous design could be a highly structured electrode, but this may be difficult to manufacture.^{8, 31} The bi-tortuous electrode design is agnostic of material selection at some level, because porous electrodes will always face diffusion limitation (in the electrolyte), regardless of the material. For this reason bi-tortuous designs have proven beneficial for a variety of active materials including Si,^{24, 32} $\text{LiMn}_x\text{Fe}_{1-x}\text{PO}_4$,³³ LiFePO_4 ,^{17, 23, 25, 31} graphite,^{20, 21, 28, 34} LiCoO_2 ,^{19, 26} and $\text{LiNi}_x\text{Mn}_y\text{Co}_{1-x-y}\text{O}_2$.^{21, 27-30} This variety of materials show that the improvement of rate performance from low tortuosity paths engineered into electrodes is not dependant on a specific material. Another approach to generate structured electrodes is to formulate the electrode slurry to control cracking in the electrode during drying, where cracks provide pathways of reduced tortuosity.^{32, 35} Scaling developments like these could be challenging,³⁶ but perhaps less so than more fundamental battery developments.³⁷ Bi-tortuous electrodes have been shown to be scalable to multi-layer pouch cells,³⁸ and laser patterning has been performed on roll-to-roll machines.³⁹ Even cracked electrodes show results repeatable across 4 sets of manufactured electrodes, despite their stochastic appearance.³⁵ Structured electrodes are a promising technology widely applicable to different materials and show signs of being scalable.

Another potential stumbling block for wide adoption of structured electrode is design, since there are several extra interrelated parameters to set. Currently, designing bi-tortuous electrode structures is based on a mixture of informed intuition and trial and error.⁴⁰ A rational design paradigm, where underlying chemistry, physics and material properties can be used to specify optimal electrode structure directly would be preferred. Image based models^{16, 41-45} can be of immense help here. They have already been applied to interpret results from structured electrodes and to optimize a proposed structure design.^{30, 44, 46, 47} However, these models are still sensitive to parameters that are difficult to measure *ex-situ* and can be non-identifiable because several underlying microstructures can produce the same electrochemical response.⁴² This makes these models difficult to apply at scale. What is required is a greater understanding of the mechanics of mass transport within the electrode, during operation. More specifically, the intersection between the feature introducing reduced vertical tortuosity and the resulting transport. This will allow for more informed intuition-based design as well as be the foundation for more accurate predictions from microscopic models via spatially resolved datasets for fitting or validation. For this purpose a model system is required, and here we use the cracked electrode³⁵. It has the advantage that it requires no extra processing, the slurry (and thus electrode properties) are homogenous. It provides vertically oriented features of low tortuosity and leaves the rest of the electrode as a typical lithium battery electrode. The focus of the present work is to study transport in structured electrodes through that model system by accessing the hidden variables by *operando* XRD.

Measurements made in specialized *operando* cells using X-rays have been invaluable in improving our understanding of batteries.⁴⁸ This is in part because it is possible to correlate unit cell parameters with the state of lithiation.⁴⁹ “Pencil beam” experiments (conventional transmission XRD with a very small



spot size) have been used to obtain XRD measurements representative of the whole path of the beam through the cell. These measurements are fast enough, but the fact that you obtain signal from the entire path of the beam restricts the kind of geometry of regions that can be compared. For example, this has been deployed successfully to study lithiation state variation versus perpendicular distance from the current collector.^{15, 50, 51} XRD-CT,^{13, 52} another candidate technique, has the advantage of being able to provide three-dimensional maps of lithiation state made with a spatial resolution determined only by the beam dimension or primary particle size.⁵² Unfortunately typical acquisition times, which could be 15 mins per slice (dependent on acquisition conditions, and size of electrodes) even at synchrotron X-ray sources are too slow to be considered *operando* at the charge/discharge rates of interest (e.g. at even ~0.5C this would far too slow).⁵⁰ An alternative method to consider for localized measurements is multi-channel collimator (MCC)-XRD. The MCC-XRD can acquire XRD patterns where the signal all comes from a specific volume in space (the gauge volume) by blocking all other paths. This approach was originally developed for conducting XRD in harsh environments,⁵³⁻⁵⁵ but has recently been applied in examining the interior temperature of 18650 batteries.⁵⁶ It provides a compromise between the speed of pencil-beam measurements and the site specificity of XRD-CT. Spatially, the diffracted rays measured in MCC-XRD come from a volume bounded by the geometry of the beam in directions perpendicular to the orientation of the beam. In this respect it is the same as pencil beam. Along the direction of the beam for the MCC-XRD the volume's length depends on the beam energy and the reflection angle but can be 0.2 -3 mm for energies and angles typically used to measure battery materials. Temporally, an MCC-XRD measurement can take ~1s, about 1000x slower than a rapid synchrotron diffraction measurement, but still fast enough for time scales involved in even high-rate battery processes. Exactly how high rate depends on how many points of MCC-XRD are required. For example, if 10 points are required this could enable *operando* characterization of a 20C cycle. Overall, it has the right blend of speed and accuracy to study lithiation at a feature size relevant to tortuosity-modified electrodes (the features must have at least one axis which it is 100s of μm long, but otherwise can be quite small) at speeds fast enough to be of interest (~1s/point). Importantly, it can probe the interior of devices non-destructively and so little to no modification of the cell is required. This can be a major advantage as reflections from the casing can be completely suppressed. This allows analysis of reflections that would normally be obscured by overlaps. MCC-XRD can be an appropriate technique when the spatial and temporal resolutions match the structures/processes under study, or when isolating signal from background is important.

In this work we utilise MCC-XRD to explore the behaviour of electrodes which have been microstructured by cracking in the electrode during drying installed in typical 2032 type coin cells as model systems to understand bi-tortuous electrode function and design better. The MCC-XRD technique allows sufficiently site specific XRD measurements which enables the direct observation of the lithiation and delithiation behaviour of active material particles near cracks in the electrode during capacity limiting cycling rates. The cracked electrodes are very appropriate for this study because they have directional tortuosity and a proven increase in discharge capacity at high rates, and the active material particles remain pristine until cycled. MCC-XRD measurements on these electrodes allow us to shed new light on the lithium-ion mass transport inside an electrode which is a key step toward establishing the rational design of tortuosity modified electrodes.

Methods & Materials

Electrode and cell manufacturing

Electrodes were manufactured following methods described in a previous publication.³⁵ A slurry was mixed in a planetary mixer (Thinky ARE-250, Intertronics) composed of NMC 622 (BASF), super C65 (IMERYS GRAPHITE & CARBON), and PVDF (Solvay) in an 87:8:5 weight ratio with a 40% solid content in N-Methyl-2-pyrrolidone (NMP). This has been shown in previous work to consistently generate



electrode crack structures.³⁵ Coatings of two different thicknesses (900 and 600 μm – wet thickness) were produced with a doctor blade and draw down coater (Elcometer 3600/4 and 4340 respectively) and dried on a hot plate at 80 $^{\circ}\text{C}$, and found to have 55% porosity. Discs of the cast electrode were cut out at 5 and 10 mm using a laser micro-machining system (Series A, Oxford Laser). The discs were circular except for two short flat, notched edges which were cut to be a right angle to each other (for use during beamline alignment). The sample location (within the macroscopic electrode sheet) was determined by use of a microscope (VHX-7000, Keyence). Long straight cracks in the electrode that appeared isolated from other cracks were screened for, and then careful measurements were taken to align the electrode sheet in the laser to extract a smaller electrode with that crack. These cracks will typically go through most of the thickness and be slightly narrower on the bottom than the top. The microscope was also used to measure the features of interest and general electrode dimensions (used during beam alignment), alongside an image analysis procedure using Ilastik⁵⁷ as previously described.

These electrode discs were assembled into half-cells in standard 2032 coin cells (Hohsen), albeit in a slightly altered configuration (see Figure S1) which has been proven to work for high rate operando XRD measurements⁵¹. Cells had spacers on both sides and the cathode side spacer was aluminium instead of the normal stainless steel. This is to ensure a flat electrode and allow x-ray escape. Additionally, the cathode was only 5-10 mm diameter instead of the normal 15 mm to allow for beam transmission optimization. Lithium discs were the normal size, removing issues of electrode alignment. Two of the assembled cells were selected for measurements at the beamline. The electrode mainly discussed here (see Figure 1 a) was selected for having particularly long and straight crack features in it and are comparable to electrodes studied in our previous work³⁵ in terms of the cracking intensity factor (the amount of the surface which is covered by cracks), coat weight and thickness (see Table 1). Another electrode was also studied (see Figure 1 b) and also had promising characteristics (see Table S1), except it was thinner and the crack was less long. Of the two electrodes that were studied, the one that is focused on here was thicker (195 μm vs 145 μm), wider (10 mm vs 5 mm diameter), and had a longer crack to focus on. Thicker electrodes are more interesting for bi-tortuous designs, larger electrodes will be more representative, which is why this electrode was focused on, and the length of the crack is important for the MCC-XRD measurements as discussed below.

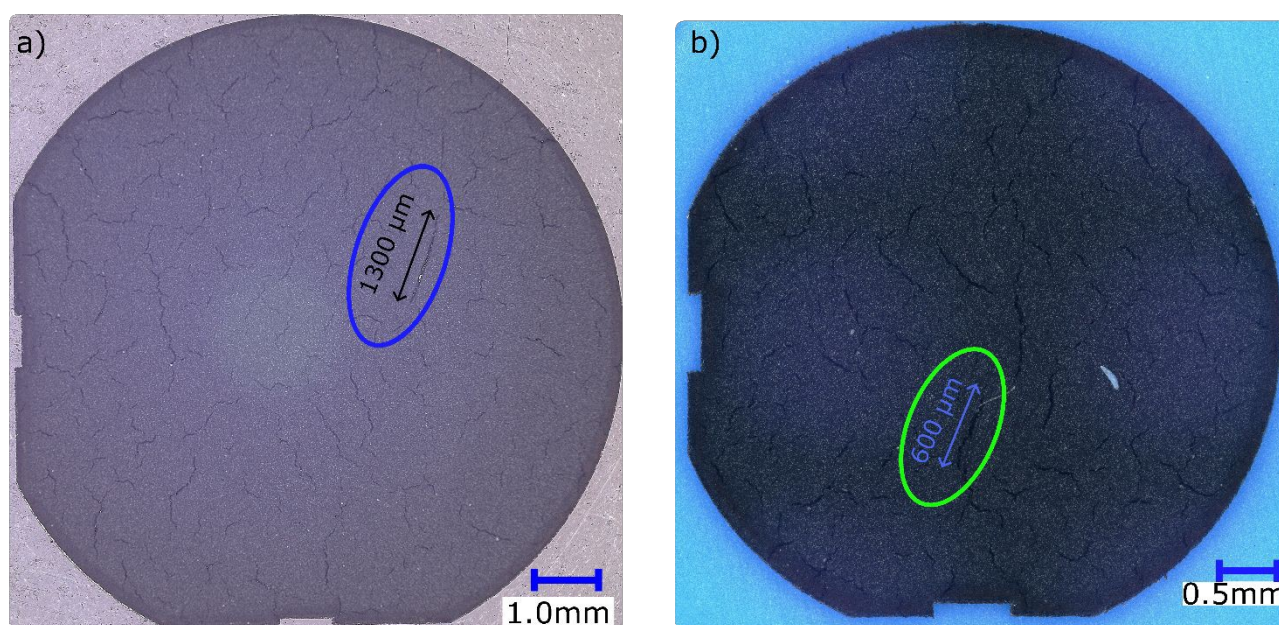


Figure 1: Micrographs of the cathode used for operando measurements discussed here a) and the electrode referred to in the SI b). The crack that was studied in this work is circled with the length noted. The crack is comparable to those seen previously and imaged in x-ray computed tomography.^{35, 58}



Table 1: The properties of the electrode in Figure 1, see also Table S1.

Electrode Radius	5mm
Crack Intensity Factor ³⁵	2.03%
NMC Loading	32 mg cm ⁻²
Wet Coat thickness	900 μm
Dry Thickness	195 μm
Crack of Interest Length	1300 μm
Crack of Interest Width	50 μm
Capacity @Formation	4.3 mAh
Specific Capacity @ Formation	170 mAh
Aerial Capacity	5.47 mAh cm ⁻²
Measurement Depths	U=25, M=80, B=135 μm

View Article Online
DOI: 10.1039/D6EB00017G

Electrochemical Tests

Electrochemical measurements and cycling were undertaken using a Biologic SP300 cycler with 10 A booster (Biologic, France). After assembly into 2032-coin cells, all cells were formed using three formation cycles consisting of a C/20 constant current charge to 4.2 V, 30 s rest, a C/20 constant current discharge to 2.5 V and a 30 s rest. Formation showed that the main cell achieved specific capacities of 97% of practical capacity of this NMC622 (175 mAh/g) as outlined in Table 1. Beyond the formation cycles the cells were only cycled on the beamline. Cells installed on the beamline were cycled at various charge and discharge rates between C/10 and 2C in a pattern of constant current charge to 4.3 V, constant voltage charge till the current decayed to 0.5 of the constant current charge rate, a rest of five minutes, followed by a constant current discharge to 2.5 V. Then the cell was then rested until the voltage recovered to 3.6 V and a second constant current discharge was applied with a lower rate at least a half the nominal rate.

MCC-XRD Measurements

The MCC-XRD measurements were performed in operando conditions at the ID15A beamline of the European Synchrotron Radiation Facility (ESRF). ID15A and the extra brilliant source are high appropriate facilities for operando experiments because of the high flux and stability of the source.⁵⁹ The beam energy was 90 KeV and the cross-sectional dimensions of the beam at the battery cell were 10 μm x10 μm. Diffraction rings produced by the gauge volume were collected using a Pilatus3 X CdTe 2M hybrid pixel detector which was 1 m from the cell. A Cr₂O₃ sample was measured prior to operando measurements for calibration. A single pattern from the MCC was collected in ~3s with an exposure time of 0.1s (the MCC must be rocked back and forth to collect an entire pattern).

The geometry of the gauge volume is determined by the geometry of the MCC and the incident beam (see Figure S2). This geometry is physically determined and, thus, stable throughout the experiment. Two dimensions of the gauge are defined by the dimensions of the beam incident on the sample (10x10 μm in this case). With this arrangement, the length of the gauge volume is defined by accepting only scattered rays which pass directly between the slits comprising the inner and outer rings distant r_1 and r_2 from the centre of the sample stage. The MCC used in this experiment made inhouse at ESRF and contains 75 slits, separated by 0.8°, with distances of 50 and 200 mm, respectively, from the sample.⁵³ The dimension of the gauge volume full-width at half-maximum along the direction of the beam (δx) is thus given:

$$\frac{a}{\left(1 - \frac{r_1}{r_2}\right) \sin 2\theta} + \frac{\delta y}{\tan 2\theta} \quad (1)$$



where a is the spacing of the inner slits and δy is the horizontal width of the pencil beam. As can be seen in Equation 1, the length of the gauge volume is different depending on the 2θ of interest. This fact has two important consequences in this work because the length of the gauge volume is important for the data interpretation, namely diffracted signal at higher 2θ originates from a smaller gauge volume, and increasing the X-ray energy lengthens the gauge volume.

The sample was aligned so that the position of a crack feature on the electrode surface was aligned with the location of the gauge volume. The cell was rotationally aligned so that the crack was parallel to the beam. In this alignment when the cell is translated perpendicular to the beam, XRD patterns can be collected from volumes of the electrode that are near to, or far from, the crack (and near or far from the current collector). In this alignment XRD measurements were taken at three different depths into the electrode, and over a distance of at least $160\ \mu\text{m}$ horizontally, stepping $10\ \mu\text{m}$ (the beam width at the sample) between each measurement (see Figure 2). The importance of the length of the gauge volume is underlined here, the shorter the gauge volume (higher 2θ reflections) the more representative of the volume near the crack the measurement can be. Too long a gauge volume (low 2θ reflections) and the measurements will be averaged with scattering from the bulk electrode.

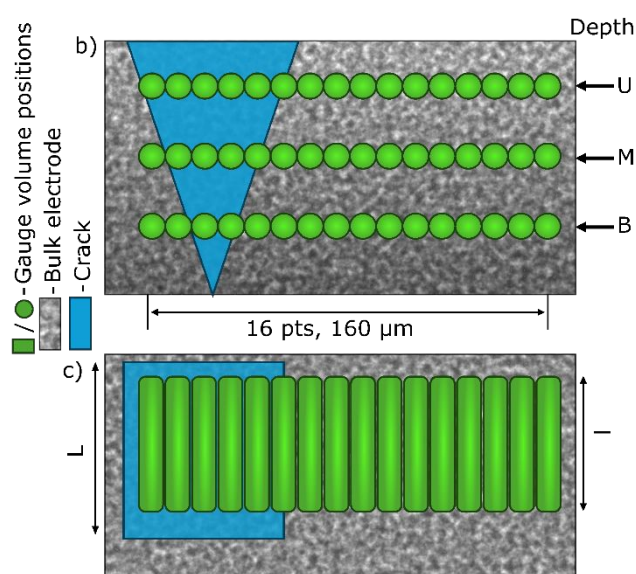


Figure 2: Schematic of MCC-XRD measurement positions relative to the crack in b) cross sectional (beam path through the page) and c) plan view beam path up and down the page. This is a schematic, the crack's position and width are not to scale, it does not narrow so much, and the boundary is not so abrupt as shown here (there is still refinable diffraction patterns even for the points full "inside" the crack", but less in counts). However, based on XRD intensities, there are approximately 6 points "in the crack" near the surface, and at the lowest depth this fell to 5 (consistent with the microscope observation). Measurements were carried out at three specific depths: upper (U), middle (M) and lower (B), and at sixteen horizontal positions. The side of the electrode closest to the separator is taken as the "top". The horizontal positions were $10\ \mu\text{m}$ wide and $10\ \mu\text{m}$ apart (directly next to each other). The crack is a length L and the gauge volume length l (depends on beam condition and 2θ angle – see MCC-XRD Measurements below).

Rietveld refinements & state of lithiation estimation

The XRD patterns were analyzed to determine the state of lithiation of the particles within the gauge volume for each measurement. First, the two dimensional diffraction patterns were integrated with pyFAI⁶⁰ to give one dimensional patterns of intensity against the 2θ angle. The one dimensional patterns were then batch refined using command line scripts and TOPAS.⁶¹ The fitted model consists of a single R-3 m phase (no other phases are present because of the nature of the MCC), with 4 Chebyshev polynomial background elements. The 2 lattice parameters a and c , scale factor, the oxygen z -position, 2 $\tan(2\theta)$ -dependent peak width parameters were refined in the model and the background elements were refined. Peak shape was also convoluted with a fixed Pseudo-Voigt contribution previously refined on the calibrant powder (Cr_2O_3). Refinement was undertaken from 2θ angles of 2.8 – 7.35° , but the lowest 2θ feature is the 104 peak at 3.3° and the highest 2θ is the 202 at 6.5° . This means the MCC gauge volume



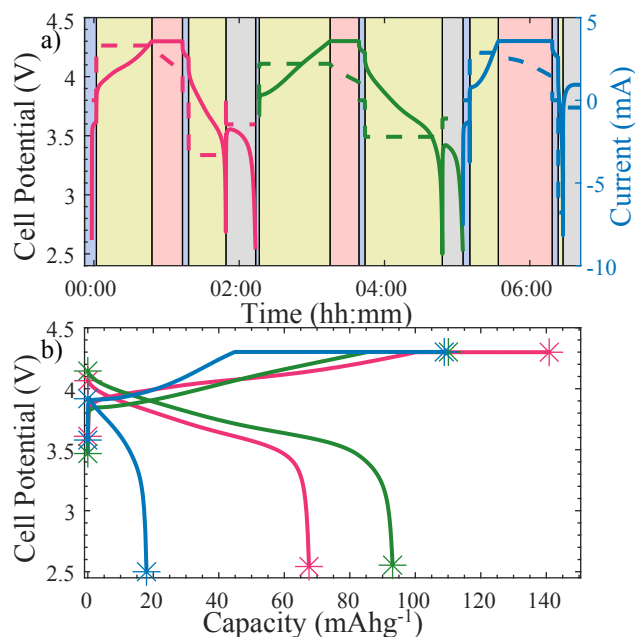
was 1.3mm long for the lowest peak and 0.67mm at the highest 2θ peak (the 202). See Figures S4-S6 for example refinements at different stages and location of the experiment and Figure S6 and Figure S7 for an examination of goodness of fit during cycling, and also Figure S8 for a pristine XRD pattern of the used material before installation in a cell. This range omits the NMC622's normally important 003 peak from the analysis because the gauge volume length for the 2θ corresponding to the 003 peak was much longer than the crack, but the remaining peaks were sufficient to refine the dimension of the unit cell. The state of lithiation (SoL) was estimated from the refined unit cell volume *via* interpolation of the data published by de Basi et al (see section S1 in the SI).⁴⁹ Refinements were also examined for just the low 2θ reflections as well as progressively higher 2θ and the derived SoL was found to be similar in each case (See section S2 and Figure S9 & S10 in the SI), demonstrating the robustness of the refinement procedure. Uncertainty bounds were calculated from the uncertainty range from the refinement, propagated through the partial derivative method of propagation (section S1 in the SI). It should be noted that it is not expected for the electrode reach 100% or 0 % SoL because of the manner of calculation arbitrarily defines these points.

Results and Discussion

Operando Cell Electrochemical Performance

Two electrodes of different thicknesses were cycled on the beamline at different rates in a standard coin cell configuration which allowed for more representative electrode sizes when compared to the bespoke *operando* cells commonly used at beamlines. The electrochemistry of both electrodes is shown in Figure 4 a and Figure S13. A good range of rates was determined by cycling 3 times and by experience with similar electrodes. On the beam it was cycled symmetrically at 0.8C, 0.5C with a final asymmetric cycle of charge at 0.65 C and discharge at 1.5C (see Figure 3). While the formation cycle reached nominal capacity (Table 1) the chosen rates were selected so that the discharge capacity would be between 25% and 75% of the full cell capacity. This shows the energy-power trade off these cells in action as fits with previous work,³⁵ and is expected based on the electrode's physical characteristics (Table 1). There is a clear trade-off between rate and capacity, which was found in previous work to be superior to the trade-off observed in non-structured electrodes of similar thicknesses. This is also observed for the thinner electrode also studied (see Figure S13). Two features of the electrochemistry that should be noted are the significant constant voltage holds which aided SoC equilibration across the different cycles following every charge cycle and the slow discharge (grey background duration on Figure 3) at half the nominal discharge rate.





View Article Online
DOI: 10.1039/D6EB00017G

Figure 3: The electrochemistry of the cells during cycling for the thicker electrode showing voltage/current vs time (left/right, solid/dotted) a), and capacity plots (b). The cycles are colour coded between a) and b) the first cycle (0.8C symmetric) is purple, the second cycle (0.5C symmetric) is green and the final cycle (0.6C charge/1.5C discharge) is blue. The background of the plot is also colour coded so that blue is open circuit, yellow is constant current, red is constant voltage, and grey is a constant current with a lower rate than the nominal rate (0.4C, 0.25C and 0.1C for each of these cycles respectively). Each cycle has a * at start and end in the capacity-potential plot (b) to help differentiate overlapping curves. For the electrochemistry of the thinner electrode see Figure S13.

Operando State of Lithiation from MCC-XRD

The direct results of the SoL analysis were found to show gradients in both the horizontal and vertical depending on the point in the cycle (see Figure 4). These trends are the interesting feature of this data, but there is also large degree of local variation. To enable engagement with the trends and remain quantitative, while minimizing the local variation, several averaged measurements were calculated. Averaging of the discrete MCC-XRD points allows for smoothing out the local variations and the identification of wider overall trends across and through the electrode.

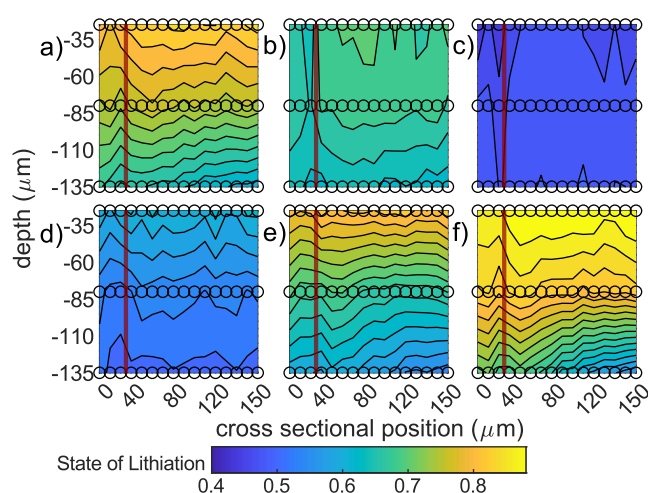


Figure 4: Contour plot the calculated SOL from the MCC-XRD measurements for the 0.8C cycle of the thick electrode (lines are contours). The crack's centre is on the left, at ~35 μm, indicated by the red line. The circles on the plot are the locations of MCC-XRD measurements, and the colour in between these points is interpolated. The graphs are of a) start of charge, b) 30 minutes into the charge, c) top of charge (1h 10m), d) 18 minutes into discharge, e) end of normal discharge, and f) 5 minutes into the slow (C/10) discharge after the normal discharge. In these plots, the SOL is interpolated between the measured positions (indicated by circles).



The data has thus been averaged in two ways. First, to examine the lateral behaviour, SoLs from gauge volumes are separated into three groups per level, namely, near crack, middle and bulk (see Figure 5 a pink, green blue, respectively), this corresponds to directly adjacent to the crack, 20-30 μm into the electrode and 100 μm in, respectively. Bulk and middle analyses are conducted using a two-point averages and the “near crack” being 5-point average because these are all points which are in/near the crack, which have sparser signal. The interpretation of does not depend on the exact points selected, which was essentially arbitrary. This can be seen in Figure S14 in the SI, which shows an alternate averaging which still maintains the overall trends. Second, for comparison of vertically oriented trends all points on each depth (bottom, near the current collector, halfway, and top, near the separator, see Figure 1 b) are averaged together (see Figure 6 , orange, purple, pink, respectively). These plots highlight several interesting features of the data, which will be examined and then discussed subsequently.

The local state of lithiation near the crack can be seen in Figure 5 for the 0.8C cycle of the thick electrode. An overall trend can be seen in which lithiation in all regions decreases from ca. 90% to 40% at top of charge. In contrast to this overlapped behaviour during charge, a clear separation of SoL can be observed during discharge. It occurs in the middle (Figure 5 a middle curves) and bottom (Figure 5 a bottom curves) layers (near the current collector) by the end of the CC discharge with this separation occurring later in the middle layer than the bottom layer by ca. 10 mins, but the final separation between the near crack and bulk is similar. This is all in direct contrast to the upper layer (Figure 4 a top curves), which shows much more even lithiation for the entire cycle and serves as an internal control.

Another important difference to note is which curves separate at which points. In the middle layer (Figure 5 a middle curves) the SoL near the crack (pink) separates from the mid position (green), indicating the particles near the crack lithiate faster, but the SoL of the mid and bulk remain overlapped – lithiating at the same rate. Contrast this with the bottom layer (Figure 5 a bottom curves) where the SoL of each horizontal positions separates. Finally, note points nearest the surface (Figure 5 a top curves) which have overlapping SoL for the entire discharge. In sum, if we consider the gradient of SoL, the bottom layer has a gradual gradient away from the crack, the middle has a gradient just slightly into the electrode from the crack and then level, and the top layer has no gradient.



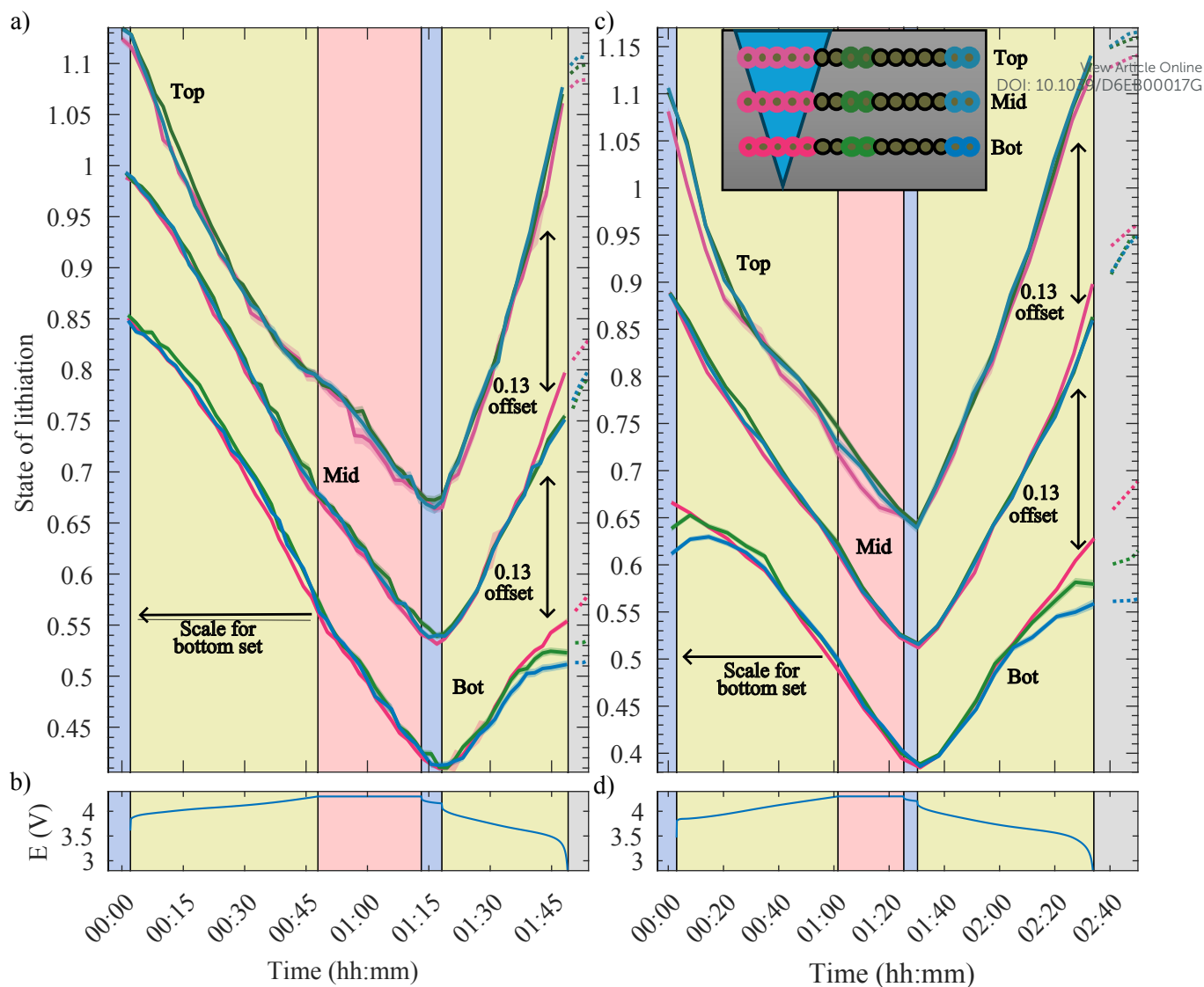


Figure 5: time evolution of the state of lithiation of different regions of the thick electrode during a) 0.8C and b) 0.5C cycles as computer from MCC-XRD measurements. In both there are 3 sets of 3 curves offset from each with the scale on the y-axis corresponding to the lowest set of curves, and each higher set of curves being off set by 0.13. See Figure S15 a-d in the SI for separate plots for each set of 3. Each curve is additionally surrounded by a confidence interval, which corresponds to the statistical uncertainty from refinement, but this is mostly hidden under the curve. The topmost group corresponds to the measurements near the surface of the electrode (labeled “Top”). The second group down corresponds to the measurements in the middle of the thickness of the electrode (labeled “Mid”). The third group down the level of measurements closest to the current collector. Each curve is the average of 2 (middle and bulk) or 5 (near crack) MCC-XRD point measurements. Inset is a schematic of the electrode cross section near the crack (as in Figure 2) with all MCC-XRD measurement points shown, and the measurement points which are plotted are highlighted with the colour corresponding to the curves. b) and d) are the voltage curve during the cycle. In all plots the background colour is synchronized to electrochemical state: Blue: Open Circuit, Yellow: constant current, pink: Constant Voltage, grey: slow CC discharge. The slow discharge in the grey is at 0.4C, which is why the SoL curves continue to separate after the end of the yellow section. The SoL curves are additionally shown in dotted during the slow discharge to distinguish them.

The results in Figure 5 c show SoL curves for the 0.5C cycle, which immediately followed the 0.8C cycle. Similar trends are seen - the SoL overlaps during charge and separates on discharge, except for the surface layer, where minimal separation (Figure 5 c top curves). However, the magnitude of separation between the SoL curves is greater at the end of discharge. Similarly, the mid level only has the near crack position lithiating faster than the bulk and the middle.

For the 0.5C cycle the separation of SoL between near the crack and the bulk at the lowest level is larger than at the middle level, contrary to the 0.8C cycle. In the 0.8C case the separation in SoL between near



the crack and the bulk is 4.5% and in the 0.5C cycle it is 7.3% for the bottom layer and 4.1% for the middle layer.

View Article Online
DOI: 10.1039/D6EB00017G

A further detail to note is that the time at which the SoL curves first separate is also different between the 0.8C and 0.5C cycles. In the 0.5C case the three SoL curves for both for middle and bottom layer separate from each other at 15 min and 30 min left in the discharge, respectively, and for 0.8C it is 8 min and 15 min. This means that the difference in the rate of change of SoL is faster in the 0.8C case, but the cycle ends faster yielding a smaller separation at the end of discharge.

A second notable difference is that the slow discharge (grey region) after the 0.8C cycle did not fully reset the electrode to a uniformly lithiated state, as differences between the positions at the lowest depth (Figure 5 c bottom curves) are apparent from the first moment of the charging cycle. This allows for observation of how uneven lithiation state at the start of charge behaves. It is apparent that the particles near the crack begin delithiation immediately, while the particles toward the bulk have either a constant SoL or a very slight amount of lithiation (the opposite of what is expected) at the start, until the SoL matches it's neighbours – mid position (green) begins delithiation when it has the SoL as that near the crack (pink), and the same for mid and bulk (blue). For this lithiation it is important to stress it is an average of all the particles in several gauge volumes which are lithiating during charge, opposite to the rest of the electrode and what is normally expected. Finally, during the slow discharge (grey region) in the bottom level the SoL of the three regions continue to separate.

The comparison of the SoL in the vertical direction for both the 0.8C and 0.5C cycles can be seen in Figure 6. Contrary to the horizontal trends, in the vertical direction the SoL do not overlap during charge. In the 0.8 C cycle (Figure 6 a), during the CC step, the top level (orange) delithiate fastest, then the middle (purple), then the bottom level (pink) slowest. When the CV step hits, the SoL curves do again overlap. Additionally, it is evident from the curvature that the top layer starts fast and slows down, the middle layer has a consistent rate, and the bottom layer starts slow and speeds up. Looking to the 0.5 C cycle (Figure 6 c) the effects of non-uniform SoL after discharge can again be seen. As in Figure 5 c bottom curves (the bottom layer during the 0.5C cycle), rate of change of SoL differs between the three levels till they reach the same SoL. Another feature of Figure 6 is the difference of SoL between the layers during discharge. The SoL of the three levels separate quickly. From the start of discharge the top layer lithiation rate is the highest overall, but the bottom layer rate also drops off at ~15 minutes. This mirrors discharge the phenomenon in Figure 5 a bottom curves.

Here, a comparison between the difference in SoL at the end of discharge between the layers (Figure 6) and horizontally (Figure 5 a) is interesting. Between the top layer and the bottom layer there is 110 μm , and between the near crack region (pink curves Figure 5) and the bulk region (blue curve Figure 5), there is 100 μm . So, although the distance is comparable, both the gradient and the absolute difference in SoL is greater vertically than horizontally. The lateral difference in SoL compared to the vertical difference is 4.5% to 27.3% (or 0.045 %/ μm to 0.25 %/ μm) and 7.3% to 27.3% (or 0.075 %/ μm to 0.25 %/ μm) for 0.8C and 0.5C respectively. For another comparison we can see a similar plot in Figure S16, showing the average SoL per depth for the thinner electrode. The distance between the top and bottom measurements is only 80 μm for this experiment. The separations are 8% (0.1 %/ μm) at 0.6C, 12 % (0.15 %/ μm) at 1.15C, 10% (0.125 %/ μm) at 1.5C and 14% (0.175 %/ μm) at 1.35C. Both the gradient and the absolute separation are smaller than the thick electrode.



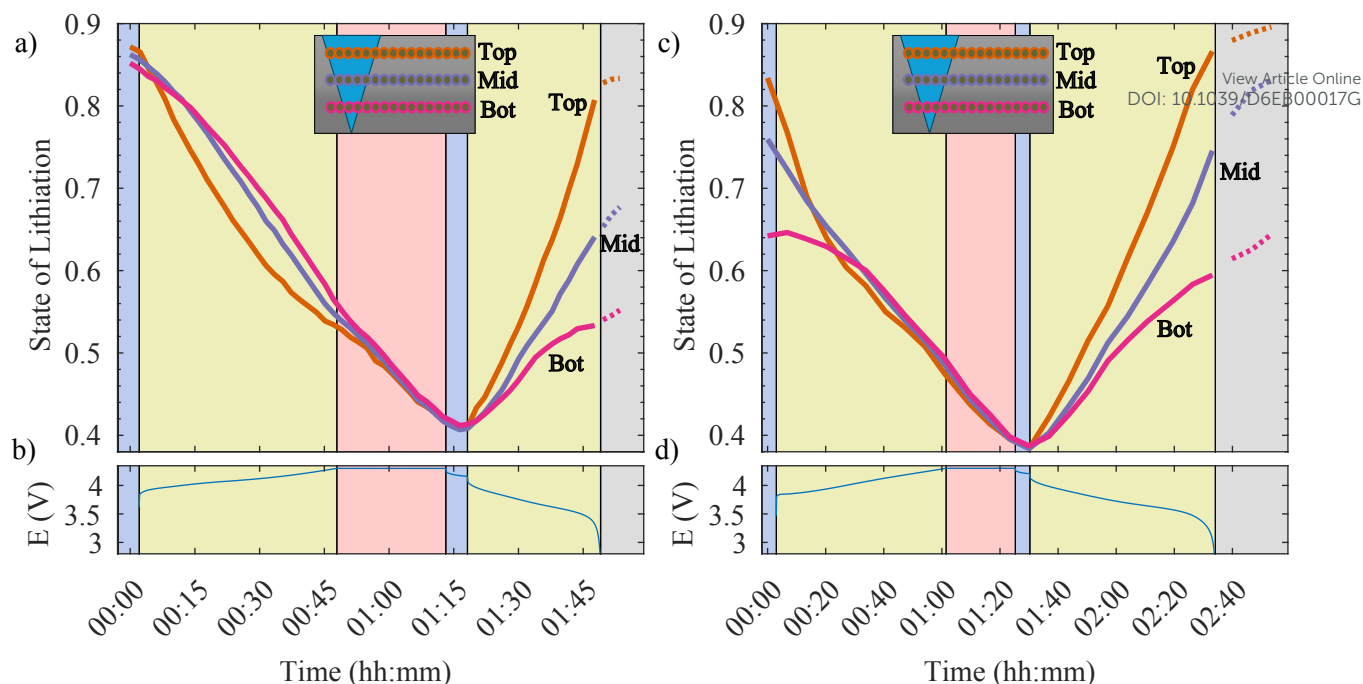


Figure 6: Time evolution of the state of lithiation of different regions of the thick electrode and the cell voltage during the a), b) 0.8C and c), d) 0.5C cycle as computed from MCC-XRD measurements. In each SoL plot the orange curve is near the surface, purple in the middle of the electrode and pink is near the bottom of the current collector. Each curve is an average all of the MCC-XRD point measurements at the specified level, this is schematically shown in e), with a schematic highlighting all the averaged points for each colour of curve (similar to Figure 2). In all plots the background colour is synchronized to electrochemical state: Blue: Open Circuit, Yellow: constant current, pink: Constant Voltage, grey: slow CC discharge. The SoL curves are additionally shown in dotted during the slow discharge to distinguish them.

The last cycle of this electrode can be seen in Figure 7, where the SoL for an asymmetric slow charge and fast discharge (followed by the normal slow discharge) can be seen. During the 1.5C discharge the top layer (Figure 7 a top curves) rapidly and evenly lithiates, the middle lithiates slightly with some separation between bulk and near the crack (Figure 7 a middle curves), and the bottom layer (Figure 7 a bottom curves) hardly starts before the cut-off voltage is reached and the cell begins the slow discharge (grey region). The top and middle layers show both show delithiation during the slow discharge (the grey background portion of Figure 7), when the electrode as a whole is lithiating. Figure 7 b compares the levels vertically – after the fast discharge during the slow discharge (grey region) the top layer delithiates ~15% of its SoL over 20 minutes of discharge before beginning to lithiate again.

Finally, a comparison can be made between this data and the thinner electrode, the full results for SoL during cycling can be seen for the thinner electrode in the supplementary information in Figure S11 and S12 (for refinements corresponding to a shorter gauge volume length). The main points observed for the thicker electrode presented here can be seen in the results from the thinner electrode, in addition to the 0.6C cycle for the thin electrode shows that at a sufficiently low cycling rate (for a given thickness) the horizontal gradients in SoL are not seen. This additional experiment, with a thinner electrode, can help show the extent to which the results examined here can be generalized.



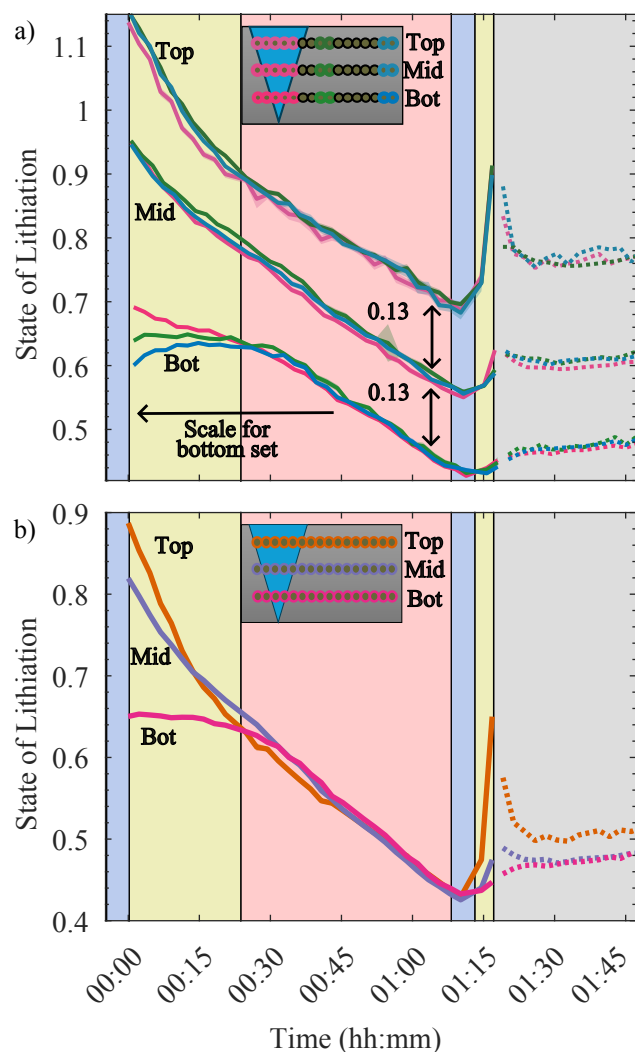


Figure 7: Time evolution of SoL in different regions for the 0.6/1.5C charge/discharge cycle of the thick electrode with lateral break down of a) the top layer, mid layer, and bottom layer, and b) the average on each layer. In a) there are 3 sets of 3 curves offset from each with the scale on the y-axis corresponding to the lowest set of curves, and each higher set of curves being off set by 0.13. Each set is a different level in the electrode the top level is the top set of curves, and the bottom level is the bottom set of curves, as also labeled on the plot. In each set the 3 curves correspond with near crack, mid and bulk positions (similar to Figure 6). This is shown schematically in the inset with highlighted colours matching the curves' colour. Each curve is additionally surrounded by a confidence interval, which corresponds to the statistical uncertainty from refinement (see section S1 in the SI). In all plots the background colour is synchronized to electrochemical state: Blue: Open Circuit, Yellow: constant current, pink: Constant Voltage, grey: slow CC discharge. The slow discharge in the grey is at 0.1C, which is why the SoL curves are slow to change in this region, except for regions with divergent current. The SoL curves are additionally shown in dotted during the slow discharge to distinguish them.

Mass transport and Electrochemistry

All of the features present in the SoL plots (Figure 5 to Figure 7) consist of various patterns of differences or similarities in the SoL of the electrode horizontally from the crack and through the thickness. An important first note is that in all cases the measurements for the level near the surface show very similar lithiation in all horizontal positions. This is expected, since, as will be seen, the effects we see in the middle and bottom layers require some diffusional path in the electrolyte. The top layer measurements are important, however, because they represent an internal control for the experiment. This is like what happens if an electrode is cycling slowly (see Figure S11a-d in the SI).

To start to explain why these are important in understanding the working of the cracked electrode as a model for general bi-tortuous electrodes we start with what a gradient in SoL in the electrode can mean.



If a gradient in SoL develops, it can indicate that a gradient in the local concentration of Li^+ ions in the electrolyte ($[\text{Li}^+]$) exists. This is because the local current density at each particle is partially depends on $[\text{Li}^+]$. If the charge transfer reaction occurs at different rates in different regions, due to differences in $[\text{Li}^+]$, the SoL in those regions will separate. Thus, the presence of an SoL gradient, as observed, can suggest some gradient in $[\text{Li}^+]$.

This points towards one explanation of one of the interesting features: the asymmetry observed in the SoL plots between charge and discharge. During discharge there is a horizontal gradient and a large vertical gradient of SoL, while during charge the horizontal gradient is non-existent (except effects from the previous cycle) and the vertical gradient is much smaller. This can all come about because of how $[\text{Li}^+]$ determines the rate of the charge transfer. There are two effects $[\text{Li}^+]$ has on local current. The first is through the equilibrium potential, which is dependent on $[\text{Li}^+]$ as can be seen through the Nernst equation⁶²⁻⁶⁵:

$$E_{cathode} = E_{cathode}^{\circ} + \frac{RT}{F} \ln \left(\frac{[\text{Li}^+](1 - [Li_p])}{[Li_p]} \right) \quad (2)$$

where $[Li_p]$ is the local concentration of lithium in the particles (as a fraction of full state of lithiation) – i.e. the SoL.⁴⁴ This effect is symmetric with respect to $[\text{Li}^+]$ and lithiation or delithiation. At high $[\text{Li}^+]$ the equilibrium potential is high, which makes lithiation easier and delithiation more difficult and vice-versa for low $[\text{Li}^+]$ causing lower equilibrium potential. Therefore, it is not likely a cause of the noted asymmetry. Secondly, $[\text{Li}^+]$ impacts the exchange current density (i_0):

$$i_0 \propto [\text{Li}^+]^{0.5} [Li_p]^{0.5} (1 - [Li_p])^{0.5} \quad (3)$$

This effect is asymmetric with respect to lithiation and delithiation, higher $[\text{Li}^+]$ resulting from poor mass transport during delithiation will inhibit delithiation through equilibrium potential but increase the rate via i_0 , but for low $[\text{Li}^+]$ delithiation is easier due to equilibrium potential, but also more difficult due to lower i_0 . Thus, all else being equal, an asymmetric response in SoL between charge and discharge is expected to a $[\text{Li}^+]$ gradient in the electrolyte. The final influence of $[\text{Li}^+]$ is through voltage gradients in the electrolyte: Li^+ mass transport limitation will lead to high resistance in the electrolyte, which can cause decreasing gradient in voltage from top to the bottom of the electrode.

Another possible cause for the asymmetry is the dependence on SoL of the diffusion constants in the active material. If the solid-state diffusion rate is lower, the (de)lithiation reaction itself will be slow, and so the dependence on mass transport in the electrolyte is reduced. The results in this study could be consistent with a lower solid state diffusion constant at low SoL, but literature reports the opposite (solid state diffusion is lower at high SoL⁶⁶), so this explanation of the asymmetry in SoL between charge and discharge unlikely. The final potential cause for the asymmetry is that the mass transport problem presented by the electrode may be inherently asymmetric. Although the paths followed by Li^+ are the same the difference is between Li^+ ions coming from several places (the AM particles) and diffusing toward one place (the separator) and vice-versa. This can be exacerbated by the dependence of the diffusion constant of Li^+ ions on $[\text{Li}^+]$,⁶⁷ and potential asymmetry in reaching the maximum $[\text{Li}^+]$ (solubility limit) or minimum $[\text{Li}^+]$ (i.e. 0). The combination of these three effects can explain the asymmetry; however, the electrochemical explanation must be said to be the most complete and likely.

The next point to discuss is the final separation of SoL after discharge (Figure 5 a&c bottom curves). A naïve explanation could be that faster rates should lead to more separation in SoL. What prevents this is the cut-off voltage. Faster (dis)charge rates do lead to greater rates of separation of SoL. This can be seen by comparing the 0.8C (Figure 5 a) to 0.5C (Figure 5 c) cycles – despite a faster rate of change in the difference of SoL between the near crack region and the bulk the total time of discharge is less, allowing the final separation to be greater in the 0.5C. The time is less not only because of the faster rate, but because the electrode reaches the cutoff potential at an earlier overall state of charge. This is



because there is a higher polarization resistance at higher current because of resistive components, but there is also likely a reactive component as well. An extreme case can also be seen in the fast discharge (Figure 7), where the middle is the only level where any lateral SoL separation is observed, and this is because the electrode hits the voltage limit almost immediately.

At this point it is interesting to discuss the capability of the channel for Li^+ transport, since this is the idea of these electrodes. It can be seen by examining one of most obvious features in all 3 cycles: that the through thickness separation of SoL (Figure 6 and Figure S16) is so much more significant compared to the horizontal separation (Figure 5 and Figure 7). The basic fact is explained by the $[\text{Li}^+]$ gradient being much higher vertically than horizontally. As estimated by the SoL, the gradient vertical is either 3x (0.5C) or 6x (0.8C) higher than horizontal. This means that in the 0.5C cycle the ratio between Li^+ transported through the crack vs the bulk is higher than at 0.8C, when it might be expected to be the opposite. The expectation could be that at high rate the bulk becomes transport limited, and more is transported through the low tortuosity crack. This explanation ignores that although inside the crack tortuosity might be seen to be 1, the transport of Li^+ is still by diffusion and will be limited by cross-sectional area. This is because a proper calculation of tortuosity is not a simple geometric calculation, but requires a simulation of diffusion.⁶⁸ In sum, at a high enough rate transport is bad everywhere, the channel does not help, so the ratio of Li^+ transported through the channel to Li^+ transported through the bulk is lower than at more marginal rates where the channel helps more. This highlights an interesting point about electrode design, any directional porosity must be designed around a target (dis)charge rate because at each rate there will be a depth at which the directional porosity ceases to assist transport.

The final matter for discussion is the points where it's apparent that the local current in some regions is divergent from the overall current density *i.e.* local lithiation during charge or vice-versa. Previously it has only been directly observed or predicted during discharge.¹⁵ In the data here it can be seen during charge in Figure 5 c, Figure 7 and slightly in Figure 6 and Figure S16. During discharge we can only see it during the slow discharge (grey region) in Figure 7. This phenomenon is more influenced by potential than mass transport. The local potential is ultimately what determines the reaction direction at any particle. It is made up from the difference of the electrolyte potential and the particle potential, and the equilibrium potential, which depends on $[\text{Li}^+]$ and the particles SoL, see eq (2). The particle potential can be approximated to be constant throughout the electrode. Not exactly true, but illustrative since the electrical resistance is much less significant than the electrolyte transport issues. The electrode potential is set to maintain the desired current and changes throughout a cycle. A particle will have a divergent current when it's SoL is different than nearby particles, so that even though the potential and the $[\text{Li}^+]$ are similar, the equilibrium potential is different. Thus, we see a divergent region first stabilize and then become typical (non-divergent) as it's SoL catches up with the local SoL like in the bottom curves in Figure 7 a during charge and this is true of the trend for the extreme result in Figure 7 b as well. The divergent current can all be viewed as the more extreme version of the different inflections in slopes of the SoL curves seen in different depths (Figure 6 a) or different horizontal positions during discharge. For the faster delithiating particles near the surface, the rate slows as the SoL decreases and $[\text{Li}^+]$ increases and for the bottom level there is an issue with too high $[\text{Li}^+]$ to start which is overcome by an increasing electrode potential. The electrochemistry cannot be ignored to explain these features.

Conclusions

In this work we have shown that MCC-XRD is a powerful tool for understanding the dynamic lithiation processes in a charging and discharging cathode in a normal coin cell, especially for patterned electrodes. We were able to monitor the local NMC particle lithiation state in *operando* measurements in a gauge volume which the electrode was moved through to map the lithiation state relative to features in the electrode. This capability is important where lateral variation in lithiation state is expected. An asymmetric charge/discharge behavior for NMC electrodes was identified which is ascribed to a combination of the effect of $[\text{Li}^+]$ on local reaction rates, the SoL dependence of solid-state lithium



diffusion coefficients, and an inherent asymmetric mass transport into vs. out of the electrode. Additionally, several unique trends in the (de)lithiation we observed which require a fully electrochemical explanation. Especially notable in this regard is locally divergent current – local delithiation when the electrode is on average lithiating and *vice-versa*. This highlights the extent to which even when focusing on the mass transport issues (such as investigating a patterned electrode) the electrochemistry cannot be neglected - a full electrochemical engineering approach is required.

These results are significant for developing a full understanding of the electrode, since they reveal a normally unobservable variable: the local lithiation state. This provides a new lens through which to think about tortuosity structured electrodes like these cracked electrodes, informing design philosophy for such electrodes. The fact that the gradient in SoL is pronounced in the vertical direction is key to understanding the dimensions that channels/holes/etc. must be to have a substantial effect on electrode performance. The asymmetric nature of delithiation and lithiation should also be considered in design and testing procedures for cathodes. It will also be valuable for modeling by increasing model parameter identifiability compared to validating against only electrochemical data, but due to the intricate nature of this work we have left it to future work.

Finally, the circumstances of divergent current regions are highlighted here, and should be considered more often in high-rate tests. The counter-intuitive result of the slower charging rate yielding more SoL separation suggests that rate-based capacity fade could be alternatively viewed as an issue of overcharging surface particles instead of a problem of mass transport to the bottom layers of the electrode.

Conflict of Interest

There are no conflicts to declare.

Acknowledgements

The authors acknowledge Beamline ID15A at The European Synchrotron (ESRF) for the experiments (ME-1650, <https://doi.esrf.fr/10.15151/ESRF-ES-1345034253>). The authors gratefully acknowledge funding from the Faraday Institution through the NEXTRODE project ((Grant FIRG015, FIRG066)), LiSTAR project (FIRG083, EP/S003053/1), degradation project (FIR0060, EP/003053/1) and the Characterisation and Manufacturing of Advanced LFP Batteries (FIRG081). P.J.W. and P.P.P. are grateful for funding by EPSRC for the International Centre to Centre Collaboration with the ESRF grant reference EP/W003333/1 and the Henry Royce Institute established through EPSRC grants EP/R00661X/1, EP/P025498/1 and EP/P025021/1. P.R.S. was supported by the Department of Science, Innovation and Technology (DSIT) and the Royal Academy of Engineering under the Chair in Emerging Technologies program (CiET1718/59). The authors would also like to thank Aimilios Davlantis Lo for last minute aluminium spacers.

Contributions

A.R.T.M. led the investigation and conceived the experiments, A.R.T.M., W.J.D., I.M., R.S.Y., A.V.L., G.G. and M.d.M. planned and prepared the experiments. A.R.T.M., W.J.D., H.T.R., J.L., and M.d.M. ran the experiments. A.R.T.M., A.V.L., and P.P.P., performed data analysis. A.R.T.M., A.V.L., A.M.B., E.K. developed the interpretation, M.D.M. leads work at ESRF as the Scientist in Charge of ID15A, E.K. leads WP2 of the NEXTRODE project, P.R.S. leads WP4 on the NEXTRODE project, A.R.T.M prepared the original manuscript, A.R.T.M., W.J.D., H.T.R., I.M., R.S.Y., A.V.L., G.G., P.P.P., A.M.B., R.J., E.K., T.S.M., J.B.R, P.J.P., D.J.L.B. and P.R.S reviewed and edited the manuscript, R.J., E.K., T.S.M., J.B.R, P.J.P., D.J.L.B. and P.R.S supervised research and acquired funding.



Data Availability

The authors affirm that the data supporting the discussion and conclusions are fully available within the article and in the SI. Raw data is available upon reasonable request.

View Article Online

DOI: 10.1039/C4EB00017G

References

1. F. Degen, M. Winter, D. Bendig and J. Tübke, *Nature Energy*, 2023, **8**, 1284-1295.
2. A. Kalair, N. Abas, M. S. Saleem, A. R. Kalair and N. Khan, *Energy Storage*, 2021, **3**, e135.
3. P. Marocco, R. Novo, A. Lanzini, G. Mattiazzo and M. Santarelli, *Journal of Energy Storage*, 2023, **57**, 106306.
4. M. Li, J. Lu, Z. Chen and K. Amine, *Advanced Materials*, 2018, **30**, 1800561.
5. M. J. Lain, J. Brandon and E. Kendrick, *Batteries*, 2019, **5**, 64.
6. H. Zheng, J. Li, X. Song, G. Liu and V. S. Battaglia, *Electrochimica Acta*, 2012, **71**, 258-265.
7. E. Catenaro, D. M. Rizzo and S. Onori, *Applied Energy*, 2021, **291**, 116473.
8. S. J. Harris and P. Lu, *The Journal of Physical Chemistry C*, 2013, **117**, 6481-6492.
9. F. P. McGrogan, S. R. Bishop, Y.-M. Chiang and K. J. Van Vliet, *Journal of The Electrochemical Society*, 2017, **164**, A3709.
10. Y. Xu, E. Hu, K. Zhang, X. Wang, V. Borzenets, Z. Sun, P. Pianetta, X. Yu, Y. Liu, X.-Q. Yang and H. Li, *ACS Energy Letters*, 2017, **2**, 1240-1245.
11. A. Singer, M. Zhang, S. Hy, D. Cela, C. Fang, T. A. Wynn, B. Qiu, Y. Xia, Z. Liu, A. Ulvestad, N. Hua, J. Wingert, H. Liu, M. Sprung, A. V. Zozulya, E. Maxey, R. Harder, Y. S. Meng and O. G. Shpyrko, *Nature Energy*, 2018, **3**, 641-647.
12. Y. Mao, X. Wang, S. Xia, K. Zhang, C. Wei, S. Bak, Z. Shadik, X. Liu, Y. Yang, R. Xu, P. Pianetta, S. Ermon, E. Stavitski, K. Zhao, Z. Xu, F. Lin, X.-Q. Yang, E. Hu and Y. Liu, *Advanced Functional Materials*, 2019, **29**, 1900247.
13. D. P. Finegan, A. Vamvakeros, C. Tan, T. M. M. Heenan, S. R. Daemi, N. Seitzman, M. Di Michiel, S. Jacques, A. M. Beale, D. J. L. Brett, P. R. Shearing and K. Smith, *Nature Communications*, 2020, **11**, 631.
14. Y. Kuang, C. Chen, D. Kirsch and L. Hu, *Advanced Energy Materials*, 2019, **9**, 1901457.
15. Z. Li, L. Yin, G. S. Mattei, M. R. Cosby, B.-S. Lee, Z. Wu, S.-M. Bak, K. W. Chapman, X.-Q. Yang, P. Liu and P. G. Khalifah, *Chemistry of Materials*, 2020, **32**, 6358-6364.
16. A. M. Boyce, X. Lu, D. J. L. Brett and P. R. Shearing, *Journal of Power Sources*, 2022, **542**, 231779.
17. C. Huang, M. Dontigny, K. Zaghbi and P. S. Grant, *Journal of Materials Chemistry A*, 2019, **7**, 21421-21431.
18. D. Kim, A. Magasinski, S.-H. Lee, H. Yoo, A.-Y. Song and G. Yushin, *Battery Energy*, *n/a*, 20230028.
19. J. S. Sander, R. M. Erb, L. Li, A. Gurijala and Y. M. Chiang, *Nature Energy*, 2016, **1**, 16099.
20. G. Zhu, D. Luo, X. Chen, J. Yang and H. Zhang, *ACS Nano*, 2023, **17**, 20850-20874.
21. J. S. Wang, P. Liu, E. Sherman, M. Verbrugge and H. Tataria, *Journal of Power Sources*, 2011, **196**, 8714-8718.
22. S. N. Lauro, J. N. Burrow and C. B. Mullins, *eScience*, 2023, **3**, 100152.
23. J. Wu, Z. Ju, X. Zhang, C. Quilty, K. J. Takeuchi, D. C. Bock, A. C. Marschilok, E. S. Takeuchi and G. Yu, *ACS Nano*, 2021, **15**, 19109-19118.
24. M. Sternad, M. Forster and M. Wilkening, *Scientific Reports*, 2016, **6**, 31712.
25. J. Wang, Q. Sun, X. Gao, C. Wang, W. Li, F. B. Holness, M. Zheng, R. Li, A. D. Price, X. Sun, T.-K. Sham and X. Sun, *ACS Applied Materials & Interfaces*, 2018, **10**, 39794-39801.
26. C.-J. Bae, C. K. Erdonmez, J. W. Halloran and Y.-M. Chiang, *Advanced Materials*, 2013, **25**, 1254-1258.
27. V. Goel, K.-H. Chen, N. P. Dasgupta and K. Thornton, *Energy Storage Materials*, 2023, **57**, 44-58.



28. N. Dunlap, D. B. Sulas-Kern, P. J. Weddle, F. Usseglio-Viretta, P. Walker, P. Todd, D. Boone, A. M. Colclasure, K. Smith, B. J. Tremolet de Villers and D. P. Finegan, *Journal of Power Sources*, 2022, **537**, 231464. View Article Online
DOI: 10.1039/D6EB00017G
29. J. Park, H. Song, I. Jang, J. Lee, J. Um, S.-g. Bae, J. Kim, S. Jeong and H.-J. Kim, *Journal of Energy Chemistry*, 2022, **64**, 93-102.
30. P. Zhu, A. Boyce, S. R. Daemi, B. Dong, Y. Chen, S. Guan, M. Crozier, Y.-L. Chiu, A. J. Davenport, R. Jervis, P. Shearing, R. N. Esfahani, P. R. Slater and E. Kendrick, *Energy Storage Materials*, 2024, **69**, 103373.
31. J. Wu, Z. Ju, X. Zhang, X. Xu, K. J. Takeuchi, A. C. Marschilok, E. S. Takeuchi and G. Yu, *ACS Nano*, 2022, **16**, 4805-4812.
32. Y. Wang, D. Dang, D. Li, J. Hu, X. Zhan and Y.-T. Cheng, *Journal of Power Sources*, 2019, **438**, 226938.
33. W. Li and W. Pfleging, presented in part at the LASE, 2026.
34. D. Kim, A. Magasinski, S.-H. Lee, H. Yoo, A.-Y. Song and G. Yushin, *Battery Energy*, 2024, **n/a**, 20230028.
35. W. J. Dawson, A. R. T. Morrison, F. Iacoviello, A. M. Boyce, G. Giri, J. Li, T. S. Miller and P. Shearing, *Batteries & Supercaps*, 2024, **7**, e202400260.
36. J.-H. Kim, N.-Y. Kim, Z. Ju, Y.-K. Hong, K.-D. Kang, J.-H. Pang, S.-J. Lee, S.-S. Chae, M.-S. Park, J.-Y. Kim, G. Yu and S.-Y. Lee, *Nature Energy*, 2025, **10**, 295-307.
37. J. Xiao, F. Shi, T. Glossmann, C. Burnett and Z. Liu, *Nature Energy*, 2023, **8**, 329-339.
38. K.-H. Chen, M. J. Namkoong, V. Goel, C. Yang, S. Kazemiabnavi, S. M. Mortuza, E. Kazyak, J. Mazumder, K. Thornton, J. Sakamoto and N. P. Dasgupta, *Journal of Power Sources*, 2020, **471**, 228475.
39. R. J. Tancin, B. Özdoğru, N. Sunderlin, P. J. Weddle, F. L. E. Usseglio-Viretta, D. R. Boone, Q. Mocaer, E. Audouard, K. W. Knehr, J. J. Kubal, S. Ahmed, D. P. Finegan and B. J. Tremolet de Villers, *EES Batteries*, 2025, **1**, 1522-1543.
40. D. Witt, D. Wilde, F. Baakes, F. Belkhir, F. Röder and U. Krewer, *Energy Technology*, 2021, **9**, 2000989.
41. A. M. Boyce, E. Martínez-Pañeda and P. R. Shearing, *Journal of Physics: Energy*, 2024, **6**, 021001.
42. R. Ge, A. M. Boyce, Y. Sun, P. R. Shearing, P. S. Grant, D. J. Cumming and R. M. Smith, *ACS Applied Materials & Interfaces*, 2023, **15**, 27809-27820.
43. F. Brosa Planella, W. Ai, A. M. Boyce, A. Ghosh, I. Korotkin, S. Sahu, V. Sulzer, R. Timms, T. G. Tranter, M. Zyskin, S. J. Cooper, J. S. Edge, J. M. Foster, M. Marinescu, B. Wu and G. Richardson, *Progress in Energy*, 2022, **4**, 042003.
44. V. P. Nemani, S. J. Harris and K. C. Smith, *Journal of The Electrochemical Society*, 2015, **162**, A1415.
45. X. Lu, A. Bertei, D. P. Finegan, C. Tan, S. R. Daemi, J. S. Weaving, K. B. O'Regan, T. M. M. Heenan, G. Hinds, E. Kendrick, D. J. L. Brett and P. R. Shearing, *Nature Communications*, 2020, **11**, 2079.
46. J.-h. Baek, H.-j. Kang, H. Kim, D. Lee and H.-K. Kim, *Journal of Power Sources*, 2025, **656**, 238052.
47. P. Zhu, B. Ebert, P. Smyrek and W. Pfleging, *Batteries*, 2024, **10**, 58.
48. A. P. Black, A. Sorrentino, F. Fauth, I. Yousef, L. Simonelli, C. Frontera, A. Ponrouch, D. Tonti and M. R. Palacín, *Chemical Science*, 2023, **14**, 1641-1665.
49. L. de Biasi, A. O. Kondrakov, H. Geßwein, T. Brezesinski, P. Hartmann and J. Janek, *The Journal of Physical Chemistry C*, 2017, **121**, 26163-26171.
50. D. P. Finegan, A. Vamvakeros, L. Cao, C. Tan, T. M. M. Heenan, S. R. Daemi, S. D. M. Jacques, A. M. Beale, M. Di Michiel, K. Smith, D. J. L. Brett, P. R. Shearing and C. Ban, *Nano Letters*, 2019, **19**, 3811-3820.
51. D. P. Finegan, A. Quinn, D. S. Wragg, A. M. Colclasure, X. Lu, C. Tan, T. M. M. Heenan, R. Jervis, D. J. L. Brett, S. Das, T. Gao, D. A. Cogswell, M. Z. Bazant, M. Di Michiel, S. Checchia, P. R. Shearing and K. Smith, *Energy & Environmental Science*, 2020, **13**, 2570-2584.
52. G. Artioli, T. Cerulli, G. Cruciani, M. C. Dalconi, G. Ferrari, M. Parisatto, A. Rack and R. Tucoulou, *Analytical and Bioanalytical Chemistry*, 2010, **397**, 2131-2136.



53. K. Yaoita, Y. Katayama, K. Tsuji, T. Kikegawa and O. Shimomura, *Review of Scientific Instruments*, 1997, **68**, 2106-2110.
54. A. Filipponi, V. M. Giordano, S. De Panfilis, A. Di Cicco, E. Principi, A. Trapananti, M. Borowski and J.-P. Itié, *Review of Scientific Instruments*, 2003, **74**, 2654-2663. View Article Online
DOI: 10.1063/1.1556017
55. G. Morard, M. Mezouar, S. Bauchau, M. Álvarez-Murga, J.-L. Hodeau and G. Garbarino, *Review of Scientific Instruments*, 2011, **82**.
56. T. M. M. Heenan, I. Mombrini, A. Llewellyn, S. Checchia, C. Tan, M. J. Johnson, A. Jnawali, G. Garbarino, R. Jervis, D. J. L. Brett, M. Di Michiel and P. R. Shearing, *Nature*, 2023, **617**, 507-512.
57. S. Berg, D. Kutra, T. Kroeger, C. N. Straehle, B. X. Kausler, C. Haubold, M. Schiegg, J. Ales, T. Beier, M. Rudy, K. Eren, J. I. Cervantes, B. Xu, F. Beuttenmueller, A. Wolny, C. Zhang, U. Koethe, F. A. Hamprecht and A. Kreshuk, *Nature Methods*, 2019, **16**, 1226-1232.
58. W. J. Dawson, A. R. T. Morrison, S. M. Tonge, M. P. Jones, K. Coke, I. C. Antony, K. Wanelik, V. Kachkanov, P. P. Paul, B. Lukić, R. S. Young, Z. Zuhair, J. Parker, I. Kesuma, G. Giri, L. Bird, A. J. E. Rettie, R. Jervis, J. B. Robinson, D. Cumming, T. S. Miller and P. R. Shearing, *EES Batteries*, 2026, DOI: 10.1039/D5EB00201J.
59. G. B. M. Vaughan, R. Baker, R. Barret, J. Bonnefoy, T. Buslaps, S. Checchia, D. Duran, F. Fihman, P. Got, J. Kieffer, S. A. J. Kimber, K. Martel, C. Morawe, D. Mottin, E. Papillon, S. Petitdemange, A. Vamvakeros, J.-P. Vieux and M. Di Michiel, *Journal of Synchrotron Radiation*, 2020, **27**, 515-528.
60. G. Ashiotis, A. Deschildre, Z. Nawaz, J. P. Wright, D. Karkoulis, F. E. Picca and J. Kieffer, *Journal of Applied Crystallography*, 2015, **48**, 510-519.
61. A. Coelho, *Journal of Applied Crystallography*, 2018, **51**, 210-218.
62. J. Hu, H. Guo, Y. Li, H. Wang, Z. Wang, W. Huang, L. Yang, H. Chen, Y. Lin and F. Pan, *Nano Energy*, 2021, **89**, 106413.
63. X. Wang and K. Aoki, *Journal of Electroanalytical Chemistry*, 2007, **604**, 101-108.
64. D. K. Karthikeyan, G. Sikha and R. E. White, *Journal of Power Sources*, 2008, **185**, 1398-1407.
65. Y. Ugata, R. Tatara, J.-y. Ock, J. Zhang, K. Ueno, M. Watanabe and K. Dokko, *The Journal of Physical Chemistry C*, 2023, **127**, 3977-3987.
66. H. Zhou, F. Xin, B. Pei and M. S. Whittingham, *ACS Energy Letters*, 2019, **4**, 1902-1906.
67. L. O. Valøen and J. N. Reimers, *Journal of The Electrochemical Society*, 2005, **152**, A882.
68. S. J. Cooper, A. Bertei, P. R. Shearing, J. A. Kilner and N. P. Brandon, *SoftwareX*, 2016, **5**, 203-210.



View Article Online
DOI: 10.1039/D6EB00017G

Data Availability

The authors affirm that the data supporting the discussion and conclusions are fully available within the article and in the SI. Raw data is also available upon reasonable request.

